Second-order topological insulators in two-dimensional monolayers of the 1T-phase PtSe$_2$ material class

Guozhi Long [1] Mingxiang Pan [1] Hui Zeng,[2] and Huaqing Huang [1,3,4]

[1]*School of Physics, Peking University, Beijing 100871, China*
[2]*State Key Laboratory of Low-Dimensional Quantum Physics, Department of Physics, Tsinghua University, Beijing 100084, China*
[3]*Collaborative Innovation Center of Quantum Matter, Beijing 100871, China*
[4]*Center for High Energy Physics, Peking University, Beijing 100871, China*

Two-dimensional (2D) second-order topological insulators (SOTIs) have been extensively studied due to their unique feature of fractional charge at corners. In order to realize such kind of SOTI in natural materials, we reveal a class of experimentally synthesized 1T-phase transition metal dichalcogenides (TMDs) monolayers as candidates of SOTI. Taking the monolayer of 1T-PtSe$_2$ as an example, we identify its second-order topology by determining the nonzero fractional corner charge using first-principles calculations and symmetry analysis. Furthermore, we emphasize the role of crystalline symmetry in the emergence of corner states based on an effective edge theory. Due to the same symmetry and similar band structure, our analysis can be directly applied to other 1T-TMD monolayers. Our findings uncover the previously overlooked higher-order topology in 2D 1T-TMD materials, which may draw immediate experimental attention.

I. INTRODUCTION

The discovery of higher-order topological insulators (HOTIs) in recent years has expanded our understanding of topological classification [1–21]. For an nth order topological insulator in d dimension, there are gapless states at its (d-n)-dimensional boundary [22,23]. In 2D materials, SOTIs have gapped states at their edges but gapless states at their corners. Different from the fact that conventional topological insulators (TIs) are protected by time-reversal symmetry, HOTIs are protected by crystalline symmetry [24] or chiral symmetry [25]. In addition, as spin-orbit coupling (SOC) is not necessary for the existence of HOTIs, it is possible to study the higher-order band topology in the spinless systems [26]. There are some bulk topological indexes to identify the second-order topology in diverse systems. For example, the $\mathbb{Z}_4$ index for HOTIs with inversion symmetry [27] is an extension of the $\mathbb{Z}_2$ index [28] for conventional TIs. Another useful indicator to identify SOTIs in 2D systems with $\mathcal{C}_n$ symmetry is the quantized fractional corner charge Q_{corner} [29]. The fractional corner charge originates from the so-called filling anomaly, which means the charge neutrality condition and crystalline symmetry can not be simultaneously satisfied under a certain number of electrons [30]. Beyond HOTIs, other higher-order topological phases such as the second-order topological superconductors have been studied in magnet-superconductor heterostructures [31–33].

Monolayers of transition metal dichalcogenides (TMD) have three common phases: 1T, 2H, and 1T′ [34,35]. Previous studies have shown that monolayers of some 2H-TMDs are SOTIs that are protected by C_3 rotation symmetry [36–38]. On the other hand, monolayers of some 1T′−TMDs have been identified as quantum spin Hall insulators which are characterized by the nontrivial Z$_2$ topology [39]. However,

less is known about the topology of monolayers of 1T-TMDs. As a representative of 1T-TMDs, monolayers of PtSe$_2$ material class [40] have attracted interest in both experimental and theoretical studies due to their excellent characteristics, such as helical spin texture [41] and unique magnetic ordering [42]. Recently, some 2D 1T-TMD films have been identified as HOTIs, which are protected by inversion symmetry and characterized by the topological $\mathbb{Z}_4$ index [43]. However, due to the improper rotation symmetry $\mathcal{S}_6$ in monolayers of the PtSe$_2$ material class, their fractional corner charge and the underlying mechanism of the second-order topology remain to be further explored.

In this work, we perform a comprehensive study on the higher-order topological characteristics of monolayers of the PtSe$_2$ material class. Based on first-principles calculations, we identify monolayer PtSe$_2$ as a SOTI, as evidenced by the quantized fractional corner charge Q_{corner} that is derived from symmetry eigenvalues at high-symmetry points in the first Brillouin zone. Moreover, we explicitly show the existence of corner states via the real-space charge distribution of the PtSe$_2$ nanodisks. To further elucidate the origin of the higher-order topological corner states, we develop an effective model to establish the bulk-edge-corner correspondence for the system, which coincides with first-principles calculations. Due to the shared crystalline symmetry and similar band structures, this analysis can be directly applied to other 2D 1T-TMD monolayers, which verifies the previously overlooked second-order topology in abundant TMD materials.

II. METHOD

We performed the first-principles calculations based on the density functional theory with the projector augmented
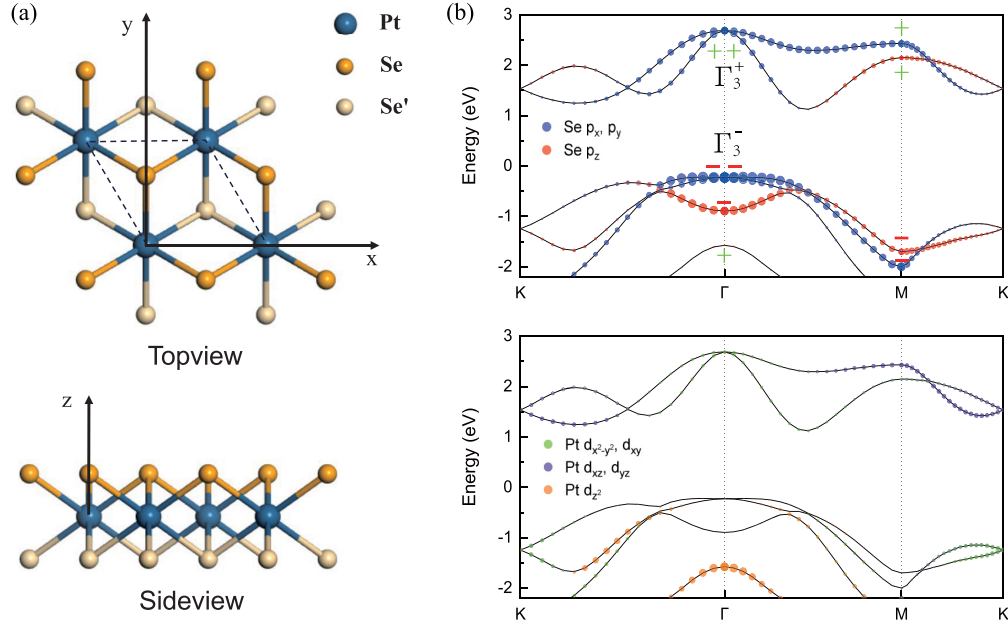
FIG. 1. Atomic and band structure of monolayer PtSe$_2$. (a) Crystal structure of monolayer PtSe$_2$ from top and side view. The symbols Se and Se$'$ denote the selenium atoms situated in the upper and lower layers, respectively. The x direction is along the twofold rotation axis of the system. The z direction is perpendicular to the atomic plane. (b) Orbital-resolved band structure of monolayer PtSe$_2$ without SOC. The size of blue and red dots represents the contribution from $p_{x,y}$, and p_z orbitals of Se atoms. $\pm$ marks Bloch states having opposite parities with respect to inversion operations at Γ and M. The size of green, violet, and orange dots represents the contribution from d_{xy,x^2-y^2}, $d_{xz,yz}$, and d_{z^2} orbitals of Pt atoms, respectively.

wave method, as implemented in the Vienna *ab initio* simulation package (VASP) [44]. The generalized-gradient approximation in the form of the Perdew-Burke-Ernzerhof functional was employed for the exchange-correlation potential [45]. The kinetic energy cutoff for plane wave expansion was set to 400 eV. The electronic structure is computed twice, one is the spinless case and the other is the spinful case with SOC. The Brillouin zone was sampled using the Monkhorst-Pack method with a $12 \times 12 \times 1$ **k**-mesh for 2D PtSe$_2$ and with a single Γ point for PtSe$_2$ nanodisks. The thickness of the vacuum layers along the z direction was set to be greater than 12 Å for 2D PtSe$_2$ and its nanodisks. The irreducible representations of electronic states were obtained by the IRVSP program [46]. We constructed maximally localized Wannier functions for Se-p and Pt-d orbitals using the Wannier90 package [47] and calculated edge states of PtSe$_2$ nanoribbons using the WannierTools package [48]. The crystal structure and charge density were plotted by VESTA [49].

III. RESULTS

A. Atomic and band structure

The physics in monolayers is essentially the same for a series of 1T-TMD materials, described below using PtSe$_2$ as an example [50,51]. Structurally, PtSe$_2$ can be regarded as strongly bonded 2D Se-Pt-Se layers that are stacked along the c axis via van der Waals interactions. Within each monolayer of PtSe$_2$, the Pt layer is sandwiched by the top and bottom Se layers, where the Pt atom is coordinated by the six neighboring Se atoms in an octahedral geometry [Fig. 1(a)]. The

monolayer of 1T-PtSe$_2$ belongs to the space group $P\bar{3}m1$ (No. 164, D_{3d}), which contains a threefold rotation along the z-axis $\mathcal{C}_{3z}$, a two-fold rotation along the x-axis $\mathcal{C}_{2x}$, an inversion $\mathcal{P}$, and an improper rotation symmetry $\mathcal{S}_6$ ($\equiv \mathcal{PC}_{6z}$).

Figure 1(b) shows the orbital-resolved band structure of monolayer PtSe$_2$ without SOC. Because the system exhibits second-order topology in the presence or absence of SOC as we discuss later, hereafter we simply focus on the spinless case without SOC for brevity, unless otherwise specified. As shown in Fig. 1(b), the monolayer PtSe$_2$ is an insulator with a band gap of 1.35 eV, which is consistent with previous studies [40,41]. The bands around the gap are dominated by the p orbitals of Se atoms and the d orbitals of Pt atoms. Due to the strong in-plane and out-of-plane anisotropy, the $p_{x,y}$ and p_z orbitals split, leaving the conduction and valence bands mainly composed of $p_{x,y}$ orbitals of Se atoms. It is noted that there are also some contributions from the Pt d_{xy} and $d_{x^2-y^2}$ orbitals in the conduction bands around Γ and the valence bands around K, implying a strong p-d hybridization because the $p_{x,y}$ orbitals on the top and bottom Se layers hybrid with the d_{xy,x^2-y^2} orbitals on the central Pt layer, which leads to an effective coupling between top and bottom Se layers and opens a large gap. As a result, both the conduction and valence bands at Γ are formed by degenerate doublet states, which corresponds to the 2D irreducible representation Γ_3^+ and Γ_3^- of the D_{3d} group, respectively.

B. Topological index

To identify the second-order topology in monolayer PtSe$_2$, we calculate the quantized fractional corner charge Q_{corner} in

TABLE I. Fractional corner charge Q_{corner} in both spinless and spinful cases and energy gap E_g (eV) of monolayers of 1T-TMDs.

	NiO$_2$	NiS$_2$	ZrS$_2$	ZrSe$_2$	HfS$_2$	HfSe$_2$	PtO$_2$	PtS$_2$	PtTe$_2$	TiS$_2$
$Q_{\text{corner}}^{\text{spinless}}$	$\frac{2}{3}e$	$\frac{2}{3}e$	$\frac{2}{3}e$	$\frac{2}{3}e$	$\frac{2}{3}e$	$\frac{2}{3}e$	$\frac{2}{3}e$	$\frac{2}{3}e$	$\frac{2}{3}e$	$\frac{2}{3}e$
$Q_{\text{corner}}^{\text{spinful}}$	$\frac{4}{3}e$	$\frac{4}{3}e$	$\frac{4}{3}e$	$\frac{4}{3}e$	$\frac{4}{3}e$	$\frac{4}{3}e$	$\frac{4}{3}e$	$\frac{4}{3}e$	$\frac{4}{3}e$	$\frac{4}{3}e$
E_g	1.41	0.48	1.12	0.46	1.30	0.61	1.81	1.84	0.79	0.06

both spinless and spinful cases. For 2D spinless insulators with $\mathcal{S}_6$ and $\mathcal{T}$ symmetries, Q_{corner} can be evaluated as [52]

$$Q_{\text{corner}}^{\text{spinless}} = \frac{e}{4}[\tilde{M}_+^{(i)}] + \frac{e}{6}[\tilde{K}_1^{(3)}] \mod e, \tag{1}$$

where $[\tilde{M}_+^{(i)}] = \#\tilde{M}_+^{(i)} - \#\tilde{\Gamma}_+^{(i)}$ is the difference in the number of occupied bands with inversion eigenvalue even between M and Γ. $[\tilde{K}_p^{(n)}] = \#\tilde{K}_p^{(n)} - \#\tilde{\Gamma}_p^{(n)}$ is the difference in the number of occupied bands with $\mathcal{C}_n$-rotation eigenvalues $\exp[\frac{2\pi i(p-1)}{n}]$ for $p = 1, 2, \ldots, n$ between K and Γ. Based on the first-principles calculations, we have $[\tilde{M}_+^{(i)}] = 0$ and $[\tilde{K}_1^{(3)}] = -2$. Therefore, $Q_{\text{corner}}^{\text{spinless}} = \frac{2}{3}e$ for monolayer PtSe$_2$ in the spinless calculations.

For the spinful case with SOC included, the formula of the corner charge Q_{corner} becomes [53]

$$Q_{\text{corner}}^{\text{spinful}} = -\frac{e}{4}[M_-^{(i)}] - \frac{e}{3}[K_2^{(3)}] \mod 2e, \tag{2}$$

where $[M_-^{(i)}]$ ($[K_2^{(3)}]$) is the difference in the number of occupied bands with $\mathcal{P}$ ($\mathcal{C}_{3z}$) eigenvalue -1 between M (K) and Γ. Our spinful calculations with SOC show that $[M_-^{(i)}] = 0$ and $[K_2^{(3)}] = 2$, which leads to $Q_{\text{corner}}^{\text{spinful}} = \frac{4}{3}e$ for monolayer PtSe$_2$ in the presence of SOC. Therefore, we verify the nontrivial second-order topological nature of monolayer PtSe$_2$ in both spinless and spinful cases.

Previous work [53] has demonstrated that there is a one-to-one mapping between the $\mathcal{C}_3$ eigenvalues of the spinful and spinless cases: $[K_2^{(3)}] = -[\tilde{K}_1^{(3)}]$. It implies that

$$\left(-\frac{e}{4}[M_-^{(i)}] - \frac{e}{3}[K_2^{(3)}]\right)/2 = \frac{e}{8}[M_+^{(i)}] + \frac{e}{6}[\tilde{K}_1^{(3)}]. \tag{3}$$

Upon introducing spin, each spinless parity contributes two spinful parities by taking into account the fact the inversion eigenvalues are equal for Kramers partners. Due to the large band gap of monolayer PtSe$_2$, the SOC cannot induce any band inversions, which yields a simple mapping between spinless and spinful parities $[M_+^{(i)}] = 2[\tilde{M}_+^{(i)}]$ due to the doubling of the number of bands. We, therefore, arrive at $Q_{\text{corner}}^{\text{spinful}} = 2Q_{\text{corner}}^{\text{spinless}}$, indicating that the doubling of the corner charges comes with going from spinless to spinful cases. Consequently, we will discuss later the formation of corner charges by constructing a spinless effective model for the sake of simplicity.

In addition to monolayer PtSe$_2$, we also examine the topological index of monolayers for a series of 1T-TMD materials through first-principles calculations. Because these materials share the same symmetry and have similar band structures, the above analysis is also applicable to them. As shown in Table I, despite different energy gaps, all of these materials exhibit

the same $Q_{\text{corner}}^{\text{spinless}} = \frac{2}{3}e$ and $Q_{\text{corner}}^{\text{spinful}} = \frac{4}{3}e$, indicating their nontrivial second-order topology. In addition, by examining the results with and without SOC, we further confirm that Q_{corner} of 1T-TMDs monolayers remain the same, which indicates the robustness of the SOTIs against the SOC effect. Noting that all the materials listed in Table I are insulators, while other 1T-TMD materials such as MoS$_2$ or CrS$_2$ are metallic in their monolayer forms and therefore, are considered here.

C. Corner and edge states

Next, we perform a first-principles calculation to directly verify the existence of corner charges. Due to filling anomaly, the fractional corner charge depends on the occupation of corner states [30]. We analyze the energy spectrum and the charge distribution of states around the Fermi level for three nanodisks with different shapes: hexagon, triangle, and rhombus. It is noted that these samples have two types of corners with angles $\frac{2\pi}{3}$ and $\frac{\pi}{3}$, respectively. As shown in Figs. 2(a) and 2(d), there are six nearly degenerate states around the Fermi level for the hexagonal nanodisk and their charges are distributed at the six corners. For the rhombus one, the charge distributions of two states around the Fermi level are mainly localized at the $\frac{2\pi}{3}$ corners, with no charge gathered at $\frac{\pi}{3}$ corners [see Figs. 2(b) and 2(e)]. Conversely, the triangle nanodisk does not exhibit localized corner charges at any $\frac{\pi}{3}$ corners [see Fig. 2(c)]. The calculated results are consistent with the symmetry requirement for the existence of fractional corner charge in $\mathcal{S}_6$-symmetric higher-order topological insulators [29,30]. Additionally, we examine the energy spectrum of PtSe$_2$ nanoribbons with zigzag and armchair edges, confirming the gapped edge spectrum, as shown in Fig. 3.

D. Effective model analysis

To reveal the underlying origin of the corner states in monolayer PtSe$_2$, we construct an effective model based on the symmetry of monolayer PtSe$_2$ and derive an edge theory to explain the nontrivial fractional corner charge. To do so, we first establish a spinless model with D_{3d} and $\mathcal{T}$ symmetries at the Γ point. The generators for the D_{3d} point group are chosen as the threefold rotation $\mathcal{C}_{3z}$, the twofold rotation $\mathcal{C}_{2x}$, and inversion $\mathcal{P}$. We consider two upper valence bands and two conduction bands near the band gap, both of which are doubly degenerate at the Γ point. Since these four bands are mainly composed of the Se $p_{x,y}$ orbitals and Pt d_{xy,x^2-y^2} orbitals, we select the following four states as the bases: $d_+ = -\frac{1}{\sqrt{2}}(d_{xy} + id_{x^2-y^2})$, $d_- = \frac{1}{\sqrt{2}}(d_{xy} - id_{x^2-y^2})$, $p_+ = -\frac{1}{\sqrt{2}}(p_x + ip_y)$, and $p_- = \frac{1}{\sqrt{2}}(p_x - ip_y)$. Therefore, the
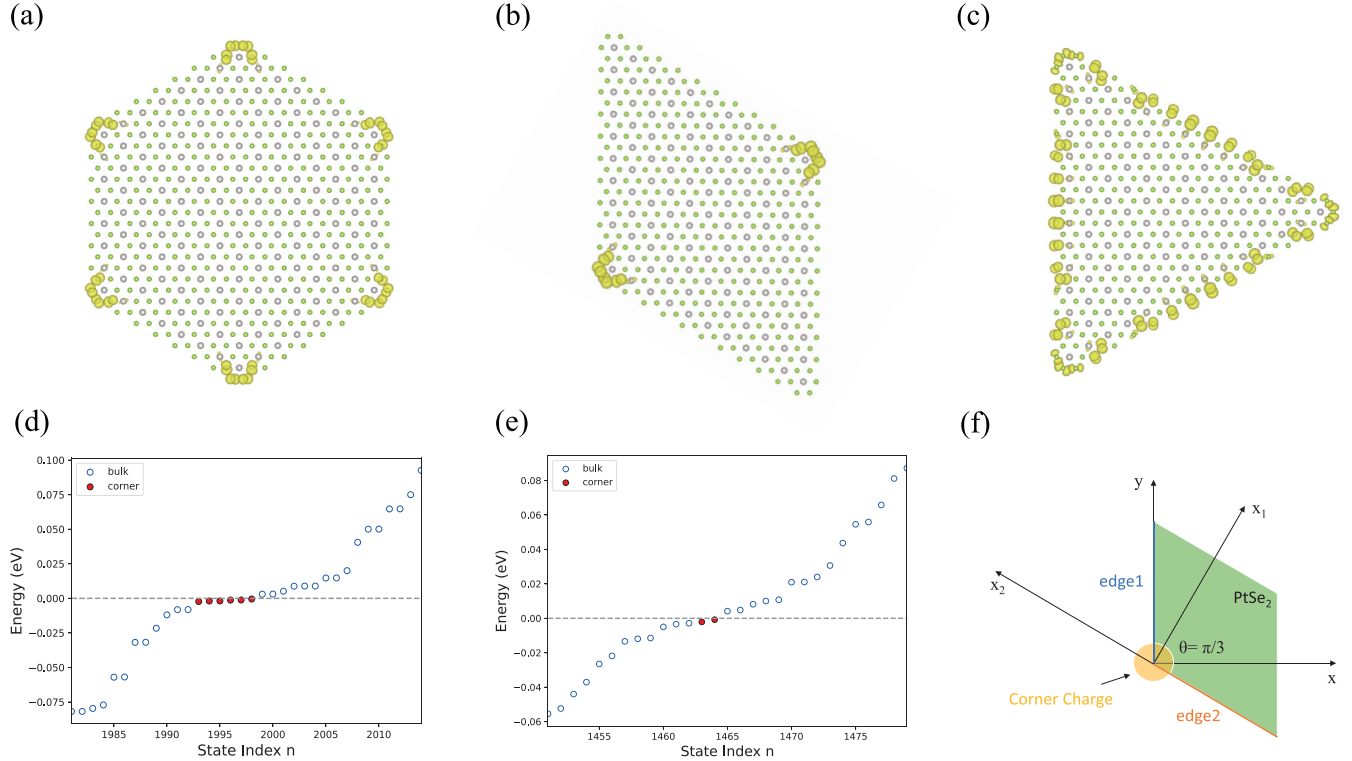
FIG. 2. Corner charges of monolayer PtSe$_2$. (a), (b), (c) Top view of the real-space charge distributions of corner states around the Fermi level for the hexagonal (553 atoms, isosurface level = 0.0006 electron bohr^{-3}), rhombus (407 atoms, isosurface level = 0.001 electron bohr^{-3}), and triangle (358 atoms, isosurface level = 0.0003 electron bohr^{-3}) nanodisks. The gray (green) balls represent Pt (Se) atoms. (d), (e) Energy spectrum of hexagonal and rhombus nanodisks. The red circles represent corner states. (f) Schematic illustration of the corner charge at the intersection of two edges. The new coordinate system x_1-x_2 is rotated counterclockwise by $\theta = \frac{\pi}{3}$ relative to the original xy coordinates. The two edges are cut along the y and x_2 axes, respectively.

symmetry operations are represented by

$$\mathcal{C}_{3z} = \begin{bmatrix} e^{i\frac{4\pi}{3}} & 0 & 0 & 0 \\ 0 & e^{-i\frac{4\pi}{3}} & 0 & 0 \\ 0 & 0 & e^{i\frac{2\pi}{3}} & 0 \\ 0 & 0 & 0 & e^{-i\frac{2\pi}{3}} \end{bmatrix}, \quad (4)$$

$$\mathcal{C}_{2x} = s_3 \otimes \tau_1, \mathcal{P} = s_3 \otimes \tau_0, \mathcal{T} = s_0 \otimes \tau_1 \mathcal{K},$$

where $\mathcal{K}$ is the complex conjugate operator. s and τ are Pauli matrices. s_0 and τ_0 are the 2×2 identity matrix. Constrained by these symmetries, the effective model expanded to k-quadratic order reads

$$\begin{aligned} H = w_0 + w_1 k^2 + (m_0 - Bk^2)s_3 \otimes \tau_0 \\ + v(k_x s_1 \otimes \tau_3 - k_y s_2 \otimes \tau_0) \\ + (k_x^2 - k_y^2)(c_1 s_0 + c_2 s_3) \otimes \tau_1 \\ + 2k_x k_y(c_1 s_3 + c_2 s_0) \otimes \tau_2. \end{aligned} \quad (5)$$

The coefficients are material-dependent parameters that can be determined by fitting the energy spectrum of the effective Hamiltonian to that of first-principles calculations. Our fitting yields $w_0 = 1.23$ eV, $w_1 = -254.76$ eVÅ^2, $m_0 = 1.46$ eV, $B = 362.22$ eVÅ^2, $v = 20.47$ eVÅ, $c_1 = 172.42$ eVÅ^2, and $c_2 = 119.28$ eVÅ^2.

Next, we derive an edge model from the effective Hamiltonian (5). Because the $w_0 + w_1 k^2$ term is an overall energy that does not affect the relative energy level, we omit this term in the following discussion for simplicity. We also neglect the last two k-quadratic terms temporarily and reintroduce them as a perturbation later. With these assumptions, the Hamiltonian is simplified as

$$\tilde{H} = (m_0 - Bk^2)s_3 \otimes \tau_0 + v(k_x s_1 \otimes \tau_3 - k_y s_2 \otimes \tau_0). \quad (6)$$

This Hamiltonian resembles the well-known Bernevig-Hughes-Zhang (BHZ) model of quantum spin Hall insulators [54], where doubly degenerate Kramers pairs exist at time-reversal-invariant momentum. However, in our spinless system, the double degeneracy only occurs at Γ and is protected by crystalline symmetry $s_3 \otimes \tau_2 \mathcal{K}$ instead of the time-reversal symmetry.

To solve the simplified Hamiltonian (6) on an arbitrary edge, we define a new coordinate system x_1-x_2, which is rotated counterclockwise by θ relative to the original x-y coordinates [see Fig. 2(f)]. The bases of the new coordinates are $\vec{e}_1 = \cos\theta \vec{e}_x + \sin\theta \vec{e}_y$ and $\vec{e}_2 = -\sin\theta \vec{e}_x + \cos\theta \vec{e}_y$. The transformations between the new coordinates and the original x-y coordinates in both spatial and momentum spaces are given by [55]

$$\begin{cases} x = x_1 \cos\theta - x_2 \sin\theta, k_x = k_1 \cos\theta - k_2 \sin\theta, \\ y = x_1 \sin\theta + x_2 \cos\theta, k_y = k_1 \sin\theta + k_2 \cos\theta. \end{cases} \quad (7)$$
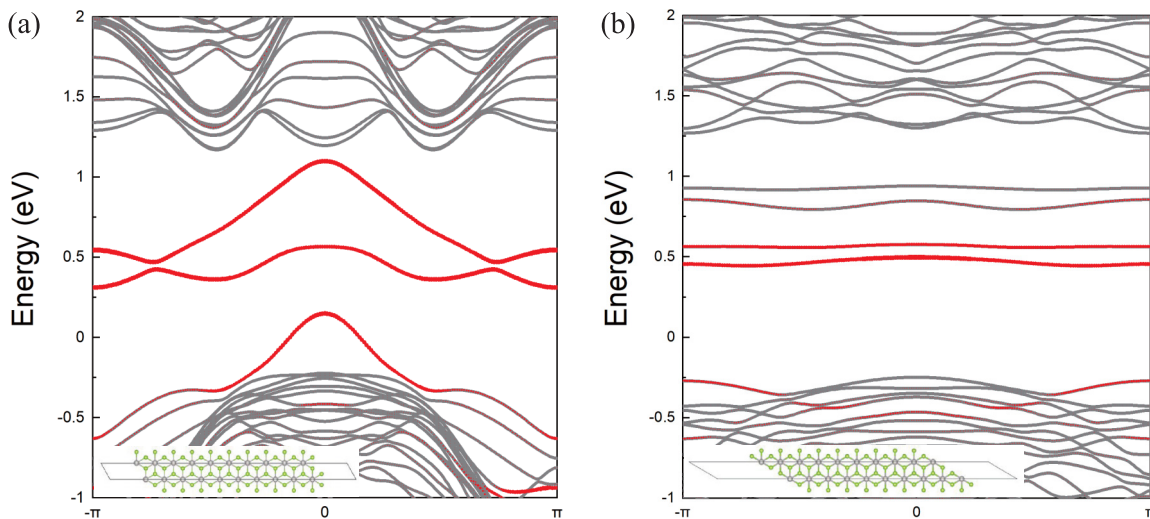
FIG. 3. Energy spectrum of PtSe$_2$ nanoribbons with (a) zigzag and (b) armchair edges. The red color represents the edge spectrum. The insets in each panel show the structure of nanoribbons from the top view.

Substituting Eq. (7) into Eq. (6), we obtain the Hamiltonian in the new coordinates,

$$\tilde{H} = (m_0 - Bk^2)s_3 \otimes \tau_0 + v(k_1 f_1 + k_2 f_2), \quad (8)$$

where $k^2 = k_1^2 + k_2^2$, $f_1 = \cos\theta s_1 \otimes \tau_3 - \sin\theta s_2 \otimes \tau_0$, and $f_2 = -\sin\theta s_1 \otimes \tau_3 - \cos\theta s_2 \otimes \tau_0$.

To further derive the effective Hamiltonian for the edge states along the $\vec{e}_2$ direction, we consider the Hamiltonian (8) on the half-space $x_1 > 0$ in the x_1-x_2 plane and make the substitution $k_1 \to -i\partial_{x_1}$ at $k_2 = 0$, which yields

$$\tilde{H}(x_1) = (m_0 + B\partial_{x_1}^2)s_3 \otimes \tau_0$$
$$- iv\partial_{x_1}(\cos\theta s_1 \otimes \tau_3 - \sin\theta s_2 \otimes \tau_0). \quad (9)$$

Solving this 1D Hamiltonian across the edge, we arrive at two zero-energy edge modes:

$$\psi_1(x_1) = C \sin(\gamma_1 x_1)e^{-\gamma_2 x_1}\begin{pmatrix} -ie^{i\theta} \\ 1 \end{pmatrix} \otimes \begin{pmatrix} 1 \\ 0 \end{pmatrix},$$

$$\psi_2(x_1) = C \sin(\gamma_1 x_1)e^{-\gamma_2 x_1}\begin{pmatrix} ie^{-i\theta} \\ 1 \end{pmatrix} \otimes \begin{pmatrix} 0 \\ 1 \end{pmatrix}, \quad (10)$$

where the normalization factor $C = \sqrt{2\gamma_2(\gamma_1^2 + \gamma_2^2)/\gamma_1^2}$, $\gamma_1 = \sqrt{\frac{m_0}{B} - \frac{v^2}{4B^2}}$, and $\gamma_2 = \frac{v}{2B}$ [56]. Note the condition for the solutions to exist is $\frac{m_0}{B} > 0$ and we also assume $\frac{v}{B} > 0$ here, which is consistent with our fitting result. By expanding Eq. (8) around $k_2 = 0$ on the bases of these two states, we obtain the 1D edge mode,

$$H_{\text{edge}} = -vk_2\sigma_3, \quad (11)$$

where σ are Pauli matrices acting on the subspace of $\{\psi_1(x_1), \psi_2(x_1)\}$.

Then, we reintroduce the last two k-quadratic terms in Eq. (5) as a perturbation and study its effect on the edge states. We perform the same rotational transformation (7) and get the

k-quadratic terms in the new coordinates

$$H_p' = (k_1^2 - k_2^2)g_1 + 2k_1k_2g_2, \quad (12)$$

where $g_1 = \cos 2\theta(c_1s_0 + c_2s_3) \otimes \tau_1 + \sin 2\theta(c_1s_3 + c_2s_0) \otimes \tau_2$ and $g_2 = -\sin 2\theta(c_1s_0 + c_2s_3) \otimes \tau_1 + \cos 2\theta(c_1s_3 + c_2s_0) \otimes \tau_2$.

In analogy to the above derivation of edge states, we found that the edge Hamiltonian (11) would generally be gapped by an effective mass term

$$H_M \approx -\frac{|\Omega|m_0}{B}(\cos\varphi\sigma_1 + \sin\varphi\sigma_2), \quad (13)$$

where $\Omega = e^{-i\varphi}|\Omega| = c_2e^{i4\theta} + ie^{i\theta}(c_1 - c_2)\sin(3\theta)$ is a Dirac mass. This effective mass term opens an edge gap proportional to $|\Omega|m_0/B$, and the phase φ determines the fractional corner charge according to Moore's theory [57]. Specifically, a mass kink arises from the effective mass term at corners between two adjacent edges, and the phase shift of $\Delta\varphi$ results in a corner state with a fractional charge of $Q_{\text{corner}} = e|\frac{\Delta\varphi}{2\pi}|$. For the hexagonal nanodisk with respect to the $\mathcal{S}_6$ symmetry [see Fig. 2(a)], the angle $\theta = \frac{n\pi}{3}$, ($n = -2, -1, 0, 1, 2, 3$). Therefore, the angle difference $\Delta\theta = \frac{\pi}{3}$ leads to $Q_{\text{corner}} = e|\frac{\Delta(4\theta)}{2\pi}| = \frac{2}{3}e$, which coincides with the topological index $Q_{\text{corner}}^{\text{spinless}}$ given by Eq. (1) for $\mathcal{S}_6$-symmetric higher-order topological insulators.

IV. CONCLUSION

We have shown SOTIs in 2D monolayers of the PtSe$_2$ material class. We prove their nontrivial second-order topology by directly calculating the fractional corner charge in both spinless and spinful cases using first-principles calculations. Based on symmetry analysis, we construct an effective model to illustrate the underlying mechanism analytically. By projecting the bulk Hamiltonian onto edges, we derive the 1D massive Dirac model for the gapped edge states and find that the k-quadratic terms in the bulk Hamiltonian induce an edge-direction dependent mass term, leading to the

emergence of fractional corner charge. Our findings not only reveal the higher-order topological properties of a large class of 1T-TMD monolayers but also greatly extend experimentally synthesizable material candidates of SOTIs. The proposed SOTIs are expected to inspire future experimental studies and the fractional corner charge can be detected by local probes such as scanning tunneling microscopy.

Note added. Recently, we became aware of independent works on arXiv [58,59], which have some overlaps with our work.

ACKNOWLEDGMENTS

APPENDIX: THE EDGE-STATE SOLUTIONS OF THE EDGE HAMILTONIAN

We consider the Hamiltonian (8) on the half-space $x_1 > 0$ in the x_1-x_2 plane and make the substitution $k_1 \rightarrow -i\partial_{x_1}$ at $k_2 = 0$, which yields

$$\tilde{H}(x_1) = \left(m_0 + B\partial_{x_1}^2\right)s_3 \otimes \tau_0$$
$$- iv\partial_{x_1}(\cos\theta s_1 \otimes \tau_3 - \sin\theta s_2 \otimes \tau_0). \quad (A1)$$

For Pauli matrix τ_3, it satisfies

$$\tau_3\begin{pmatrix}1\\0\end{pmatrix} = \begin{pmatrix}1\\0\end{pmatrix}, \quad \tau_3\begin{pmatrix}0\\1\end{pmatrix} = -\begin{pmatrix}0\\1\end{pmatrix}. \quad (A2)$$

Therefore, the Hamiltonian (A1) can be solved within the subspace of different eigenvalues of τ_3. For the subspace with τ_3 eigenvalue 1,

$$\tilde{H}_1(x_1) = \left(m_0 + B\partial_{x_1}^2\right)s_3 - i\partial_{x_1}v(\cos\theta s_1 - \sin\theta s_2). \quad (A3)$$

Because this Hamiltonian has particle-hole symmetry, we expect that a special edge state with $E = 0$ can exist, i.e., $\tilde{H}_1(x_1)\psi(x_1) = 0$. Suppose $\psi(x_1) = e^{\lambda x_1}\phi$, we have

$$[(m_0 + B\lambda^2) + \lambda v(\cos\theta s_2 + \sin\theta s_1)]\phi = 0. \quad (A4)$$

Therefore, ϕ is the eigenstate of $t = (\cos\theta s_2 + \sin\theta s_1)$ and we can define $t\phi_\pm = \pm\phi_\pm$. The general solution is

$$\psi(x_1) = (ae^{\lambda_1 x_1} + be^{\lambda_2 x_1})\phi_- + (ce^{-\lambda_1 x_1} + de^{-\lambda_2 x_1})\phi_+, \quad (A5)$$

where $\lambda_{1,2} = \frac{v \pm \sqrt{v^2 - 4Bm_0}}{2B}$, $\lambda_1 + \lambda_2 = \frac{v}{B}$, and $\lambda_1\lambda_2 = \frac{m_0}{B}$. The coefficients a, b, c, and d can be determined by imposing the open boundary condition $\psi(0) = 0$. Together with the normalizability of the wave function in the region $x_1 > 0$, we have the condition for the existence of edge states: $\text{Re}(\lambda_{1,2}) < 0$ ($c = d = 0$) or $\text{Re}(\lambda_{1,2}) > 0$ ($a = b = 0$). The condition can only be satisfied when $\frac{m_0}{B} > 0$, which is the band inversion condition for the BHZ-like model. Moreover, when $\frac{v}{B} < 0$, we have $\text{Re}(\lambda_{1,2}) < 0$, while when $\frac{v}{B} > 0$, we have $\text{Re}(\lambda_{1,2}) > 0$. Therefore, the wave function for the edge states at the $k_2 = 0$

point is given by

$$\psi(x_1) = \begin{cases} a(e^{\lambda_1 x_1} - e^{\lambda_2 x_1})\phi_-, & \frac{v}{B} < 0, \\ c(e^{-\lambda_1 x_1} - e^{-\lambda_2 x_1})\phi_+, & \frac{v}{B} > 0. \end{cases} \quad (A6)$$

On the other hand, for the subspace with τ_3 eigenvalue -1, we have

$$\tilde{H}_2(x_1) = \left(m_0 + B\partial_{x_1}^2\right)s_3 + i\partial_{x_1}v(\cos\theta s_1 + \sin\theta s_2). \quad (A7)$$

Supposing this is a zero-energy state $\psi(x_1) = e^{\lambda x_1}\phi'$, satisfying $\tilde{H}_2(x_1)\psi(x_1) = 0$, we arrive at

$$[(m_0 + B\lambda^2) + \lambda v(-\cos\theta s_2 + \sin\theta s_1)]\phi' = 0. \quad (A8)$$

Therefore, ϕ' is the eigenstate of $t' = (-\cos\theta s_2 + \sin\theta s_1)$ and we can define $t'\phi'_\pm = \pm\phi'_\pm$. The solution is (with the same definition of $\lambda_{1,2}$ and condition $\frac{m_0}{B} > 0$)

$$\psi(x_1) = \begin{cases} a(e^{\lambda_1 x_1} - e^{\lambda_2 x_1})\phi'_-, & \frac{v}{B} < 0, \\ c(e^{-\lambda_1 x_1} - e^{-\lambda_2 x_1})\phi'_+, & \frac{v}{B} > 0. \end{cases} \quad (A9)$$

We specify ϕ_+, ϕ'_+ as

$$\phi_+ = \frac{1}{\sqrt{2}}\begin{pmatrix} -ie^{i\theta} \\ 1 \end{pmatrix},$$

$$\phi'_+ = \frac{1}{\sqrt{2}}\begin{pmatrix} ie^{-i\theta} \\ 1 \end{pmatrix}, \quad (A10)$$

and further define $\gamma_1 = \sqrt{\frac{m_0}{B} - \frac{v^2}{4B^2}}$, $\gamma_2 = \frac{v}{2B}$ [56], then $\lambda_1 = \gamma_2 + i\gamma_1$, $\lambda_2 = \gamma_2 - i\gamma_1$. Without loss of generality, we suppose $\frac{v}{B} > 0$, then there are two zero energy solutions in total,

$$\psi_1(x_1) = C\sin(\gamma_1 x_1)e^{-\gamma_2 x_1}\begin{pmatrix} -ie^{i\theta} \\ 1 \end{pmatrix} \otimes \begin{pmatrix} 1 \\ 0 \end{pmatrix},$$

$$\psi_2(x_1) = C\sin(\gamma_1 x_1)e^{-\gamma_2 x_1}\begin{pmatrix} ie^{-i\theta} \\ 1 \end{pmatrix} \otimes \begin{pmatrix} 0 \\ 1 \end{pmatrix}, \quad (A11)$$

where the normalization factor $C = \sqrt{2\gamma_2(\gamma_1^2 + \gamma_2^2)/\gamma_1^2}$.

Around $k_2 = 0$, considering the linear term $H_p = vk_2 f_2$ as perturbation and neglecting the k_2^2 term, the projected Hamiltonian on the edge can be obtained by

$$H_{\text{edge}}^{\alpha\beta}(k_2) = \int_0^{+\infty} dx_1 \psi_\alpha^*(x_1)H_p\psi_\beta(x_1), \quad (A12)$$

where $\alpha, \beta = 1, 2$. Therefore, we get the effective Hamiltonian for gapless edge states

$$H_{\text{edge}} = -vk_2\sigma_3, \quad (A13)$$

where $\boldsymbol{\sigma}$ are Pauli matrices acting on the subspace of $\{\psi_1(x_1), \psi_2(x_1)\}$.

To get second-order topology, we need to open the gap by a mass term. The last k-quadratic terms in the bulk Hamiltonian which we have dropped out before play the role of the mass term. They break the crystalline symmetry $s_3 \otimes \tau_2\mathcal{K}$ and thus split the double degeneracy of original bands. By reintroducing them back and performing the same rotational transformation (7), we get the k-quadratic terms in the new coordinates,

$$H'_p = \left(k_1^2 - k_2^2\right)g_1 + 2k_1 k_2 g_2, \quad (A14)$$

where $g_1 = \cos 2\theta(c_1 s_0 + c_2 s_3) \otimes \tau_1 + \sin 2\theta(c_1 s_3 + c_2 s_0) \otimes \tau_2$ and $g_2 = -\sin 2\theta(c_1 s_0 + c_2 s_3) \otimes \tau_1 + \cos 2\theta(c_1 s_3 + c_2 s_0) \otimes \tau_2$. Here we also replace k_1 by $-i\partial_{x_1}$ and neglect the unimportant k_2^2 term, then

$$H'_p = -\partial_{x_1}^2 g_1 - 2i\partial_{x_1} k_2 g_2. \tag{A15}$$

In the same way as Eq. (A12), we eventually get the expression of the mass term

$$H_M \approx -\frac{m_0}{B}\begin{bmatrix} 0 & \Omega \\ \Omega^* & 0 \end{bmatrix}, \tag{A16}$$

where $\Omega = c_2 e^{i4\theta} + ie^{i\theta}(c_1 - c_2)\sin 3\theta$.

[1] F. Schindler, A. M. Cook, M. G. Vergniory, Z. Wang, S. S. P. Parkin, B. A. Bernevig, and T. Neupert, Higher-order topological insulators, Sci. Adv. **4**, eaat0346 (2018).

[2] J. Langbehn, Y. Peng, L. Trifunovic, F. von Oppen, and P. W. Brouwer, Reflection-symmetric second-order topological insulators and superconductors, Phys. Rev. Lett. **119**, 246401 (2017).

[3] F. Schindler, Z. Wang, M. G. Vergniory, A. M. Cook, A. Murani, S. Sengupta, A. Y. Kasumov, R. Deblock, S. Jeon, I. Drozdov, H. Bouchiat, S. Guéron, A. Yazdani, B. A. Bernevig, and T. Neupert, Higher-order topology in bismuth, Nat. Phys. **14**, 918 (2018).

[4] C. Yue, Y. Xu, Z. Song, H. Weng, Y.-M. Lu, C. Fang, and X. Dai, Symmetry-enforced chiral hinge states and surface quantum anomalous hall effect in the magnetic axion insulator $Bi_{2-x}Sm_xSe_3$, Nat. Phys. **15**, 577 (2019).

[5] Y. Xu, Z. Song, Z. Wang, H. Weng, and X. Dai, Higher-order topology of the axion insulator $EuIn_2As_2$, Phys. Rev. Lett. **122**, 256402 (2019).

[6] R.-X. Zhang, F. Wu, and S. Das Sarma, Möbius insulator and higher-order topology in $MnBi_{2n}Te_{3n+1}$, Phys. Rev. Lett. **124**, 136407 (2020).

[7] X.-L. Sheng, C. Chen, H. Liu, Z. Chen, Z.-M. Yu, Y. X. Zhao, and S. A. Yang, Two-dimensional second-order topological insulator in graphdiyne, Phys. Rev. Lett. **123**, 256402 (2019).

[8] E. Lee, R. Kim, J. Ahn, and B.-J. Yang, Two-dimensional higher-order topology in monolayer graphdiyne, npj Quantum Mater. **5**, 1 (2020).

[9] B. Liu, G. Zhao, Z. Liu, and Z. Wang, Two-dimensional quadrupole topological insulator in γ-Graphyne, Nano Lett. **19**, 6492 (2019).

[10] M. J. Park, Y. Kim, G. Y. Cho, and S. Lee, Higher-order topological insulator in twisted bilayer graphene, Phys. Rev. Lett. **123**, 216803 (2019).

[11] B. Liu, L. Xian, H. Mu, G. Zhao, Z. Liu, A. Rubio, and Z. F. Wang, Higher-order band topology in twisted moiré superlattice, Phys. Rev. Lett. **126**, 066401 (2021).

[12] H. Huang and F. Liu, Higher-order topology induced by structural buckling, Natl. Sci. Rev. **9**, nwab170 (2022).

[13] M. Pan, D. Li, J. Fan, and H. Huang, Two-dimensional stiefel-whitney insulators in liganded xenes, npj Comput. Mater. **8**, 1 (2022).

[14] M. Pan and H. Huang, Phononic stiefel-whitney topology with corner vibrational modes in two-dimensional Xenes and ligand-functionalized derivatives, Phys. Rev. B **106**, L201406 (2022).

[15] M. Ezawa, Higher-order topological insulators and semimetals on the breathing kagome and pyrochlore lattices, Phys. Rev. Lett. **120**, 026801 (2018).

[16] F. Liu, H.-Y. Deng, and K. Wakabayashi, Helical topological edge states in a quadrupole phase, Phys. Rev. Lett. **122**, 086804 (2019).

[17] Z. Wang, B. J. Wieder, J. Li, B. Yan, and B. A. Bernevig, Higher-order topology, monopole nodal lines, and the origin of large Fermi arcs in transition metal dichalcogenides XTe_2 (X = Mo, W), Phys. Rev. Lett. **123**, 186401 (2019).

[18] C.-H. Hsu, X. Zhou, T.-R. Chang, Q. Ma, N. Gedik, A. Bansil, S.-Y. Xu, H. Lin, and L. Fu, Topology on a new facet of bismuth, Proc. Natl. Acad. Sci. USA **116**, 13255 (2019).

[19] Y. Ren, Z. Qiao, and Q. Niu, Engineering corner states from two-dimensional topological insulators, Phys. Rev. Lett. **124**, 166804 (2020).

[20] C. Chen, Z. Song, J.-Z. Zhao, Z. Chen, Z.-M. Yu, X.-L. Sheng, and S. A. Yang, Universal approach to magnetic second-order topological insulator, Phys. Rev. Lett. **125**, 056402 (2020).

[21] H. Mu, G. Zhao, H. Zhang, and Z. Wang, Antiferromagnetic second-order topological insulator with fractional mass-kink, npj Comput. Mater. **8**, 82 (2022).

[22] W. A. Benalcazar, B. A. Bernevig, and T. L. Hughes, Quantized electric multipole insulators, Science **357**, 61 (2017).

[23] W. A. Benalcazar, B. A. Bernevig, and T. L. Hughes, Electric multipole moments, topological multipole moment pumping, and chiral hinge states in crystalline insulators, Phys. Rev. B **96**, 245115 (2017).

[24] Z. Song, Z. Fang, and C. Fang, $(d-2)$-Dimensional Edge States of Rotation Symmetry Protected Topological States, Phys. Rev. Lett. **119**, 246402 (2017).

[25] R. Okugawa, S. Hayashi, and T. Nakanishi, Second-order topological phases protected by chiral symmetry, Phys. Rev. B **100**, 235302 (2019).

[26] A. Alexandradinata, C. Fang, M. J. Gilbert, and B. A. Bernevig, Spin-orbit-free topological insulators without time-reversal symmetry, Phys. Rev. Lett. **113**, 116403 (2014).

[27] Z. Song, T. Zhang, and C. Fang, Diagnosis for nonmagnetic topological semimetals in the absence of spin-orbital coupling, Phys. Rev. X **8**, 031069 (2018).

[28] L. Fu and C. L. Kane, Topological insulators with inversion symmetry, Phys. Rev. B **76**, 045302 (2007).

[29] R. Takahashi, T. Zhang, and S. Murakami, General corner charge formula in two-dimensional C_n-symmetric higher-order topological insulators, Phys. Rev. B **103**, 205123 (2021).

[30] W. A. Benalcazar, T. Li, and T. L. Hughes, Quantization of fractional corner charge in C_n-symmetric higher-order topological crystalline insulators, Phys. Rev. B **99**, 245151 (2019).

[31] P. Chatterjee, A. K. Ghosh, A. K. Nandy, and A. Saha, Second-order topological superconductor via noncollinear magnetic texture, Phys. Rev. B **109**, L041409 (2024).

[32] T. Liu, J. J. He, and F. Nori, Majorana corner states in a two-dimensional magnetic topological insulator on a high-temperature superconductor, Phys. Rev. B **98**, 245413 (2018).

[33] Z. Yan, F. Song, and Z. Wang, Majorana corner modes in a high-hemperature platform, Phys. Rev. Lett. **121**, 096803 (2018).

[34] M. Chhowalla, H. S. Shin, G. Eda, L.-J. Li, K. P. Loh, and H. Zhang, The chemistry of two-dimensional layered transition metal dichalcogenide nanosheets, Nat. Chem. **5**, 263 (2013).

[35] S. Manzeli, D. Ovchinnikov, D. Pasquier, O. V. Yazyev, and A. Kis, 2D transition metal dichalcogenides, Nat. Rev. Mater. **2**, 17033 (2017).

[36] J. Zeng, H. Liu, H. Jiang, Q.-F. Sun, and X. C. Xie, Multiorbital model reveals a second-order topological insulator in 1H transition metal dichalcogenides, Phys. Rev. B **104**, L161108 (2021).

[37] S. Qian, G.-B. Liu, C.-C. Liu, and Y. Yao, C_n-symmetric higher-order topological crystalline insulators in atomically thin transition metal dichalcogenides, Phys. Rev. B **105**, 045417 (2022).

[38] J. Jung and Y.-H. Kim, Hidden breathing kagome topology in hexagonal transition metal dichalcogenides, Phys. Rev. B **105**, 085138 (2022).

[39] X. Qian, J. Liu, L. Fu, and J. Li, Quantum spin hall effect in two-dimensional transition metal dichalcogenides, Science **346**, 1344 (2014).

[40] Y. Wang, L. Li, W. Yao, S. Song, J. T. Sun, J. Pan, X. Ren, C. Li, E. Okunishi, Y.-Q. Wang *et al.*, Monolayer PtSe$_2$, A new semiconducting transition-metal-dichalcogenide, epitaxially grown by direct selenization of Pt, Nano Lett. **15**, 4013 (2015).

[41] W. Yao, E. Wang, H. Huang, K. Deng, M. Yan, K. Zhang, K. Miyamoto, T. Okuda, L. Li, Y. Wang, *et al.*, Direct observation of spin-layer locking by local Rashba effect in monolayer semiconducting PtSe$_2$ film, Nat. Commun. **8**, 14216 (2017).

[42] A. Avsar, C.-Y. Cheon, M. Pizzochero, M. Tripathi, A. Ciarrocchi, O. V. Yazyev, and A. Kis, Probing magnetism in atomically thin semiconducting PtSe$_2$, Nat. Commun. **11**, 4806 (2020).

[43] M. Costa, B. Focassio, L. M. Canonico, T. P. Cysne, G. R. Schleder, R. B. Muniz, A. Fazzio, and T. G. Rappoport, Connecting higher-order topology with the orbital hall effect in monolayers of transition metal dichalcogenides, Phys. Rev. Lett. **130**, 116204 (2023).

[44] G. Kresse and J. Furthmüller, Efficiency of ab-initio total energy calculations for metals and semiconductors using a plane-wave basis set, Comput. Mater. Sci. **6**, 15 (1996).

[45] J. P. Perdew, K. Burke, and M. Ernzerhof, Generalized gradient approximation made simple, Phys. Rev. Lett. **77**, 3865 (1996).

[46] J. Gao, Q. Wu, C. Persson, and Z. Wang, Irvsp: To obtain irreducible representations of electronic states in the VASP, Comput. Mater. Sci. **261**, 107760 (2021).

[47] N. Marzari, A. A. Mostofi, J. R. Yates, I. Souza, and D. Vanderbilt, Maximally localized wannier functions: theory and applications, Rev. Mod. Phys. **84**, 1419 (2012).

[48] Q. Wu, S. Zhang, H.-F. Song, M. Troyer, and A. A. Soluyanov, WannierTools : An open-source software package for novel topological materials, Comput. Phys. Commun. **224**, 405 (2018).

[49] K. Momma and F. Izumi, VESTA 3 for three-dimensional visualization of crystal, volumetric and morphology data, J. Appl. Crystallogr. **44**, 1272 (2011).

[50] H. Huang, S. Zhou, and W. Duan, Type-II Dirac fermions in the **PtSe$_2$** class of transition metal dichalcogenides, Phys. Rev. B **94**, 121117 (2016).

[51] M. Yan, H. Huang, K. Zhang, E. Wang, W. Yao, K. Deng, G. Wan, H. Zhang, M. Arita, H. Yang, *et al.*, Lorentz-violating type-II Dirac fermions in transition metal dichalcogenide PtTe$_2$, Nat. Commun. **8**, 257 (2017).

[52] S. K. Radha and W. R. L. Lambrecht, Buckled honeycomb antimony: Higher order topological insulator and its relation to the Kekulé lattice, Phys. Rev. B **102**, 115104 (2020).

[53] F. Schindler, M. Brzezińska, W. A. Benalcazar, A. Bouhon, S. S. Tsirkin, M. G. Vergniory, and T. Neupert, Fractional corner charges in spin-orbit coupled crystals, Phys. Rev. Res. **1**, 033074 (2019).

[54] B. A. Bernevig, T. L. Hughes, and S.-C. Zhang, Quantum spin hall effect and topological phase transition in hgte quantum wells, Science **314**, 1757 (2006).

[55] C. Wang, F. Liu, and H. Huang, Effective model for fractional topological corner modes in quasicrystals, Phys. Rev. Lett. **129**, 056403 (2022).

[56] Y. Zhong-Bo, Higher-order topological insulators and superconductors, Acta Phys. Sin. **68**, 226101 (2019).

[57] Y.-Q. Wang and J. E. Moore, Boundary edge networks induced by bulk topology, Phys. Rev. B **99**, 155102 (2019).

[58] O. Arroyo-Gascon, S. Bravo, L. Chico, and M. Pacheco, Fractional corner charges induced by fragile topology in threefold symmetric two-dimensional materials, arXiv:2312.09240.

[59] H. Sheng, Y. Xie, Q. Wu, H. Weng, X. Dai, B. A. Bernevig, Z. Fang, and Z. Wang, Majorana corner modes in unconventional monolayers of 1T-PtSe$_2$ family, arXiv:2308.12055.